Engineering 23 (2023) 181–195

Contents lists available at ScienceDirect

Engineering

journal homepage: www.elsevier.com/locate/eng

Research
Additive Manufacturing—Article

Predictions of Additive Manufacturing Process Parameters and Molten Pool Dimensions with a Physics-Informed Deep Learning Model

Mingzhi Zhao, Huiliang Wei *, Yiming Mao, Changdong Zhang, Tingting Liu, Wenhe Liao *

School of Mechanical Engineering, Nanjing University of Science and Technology, Nanjing 210094, China

ARTICLE INFO

Article history:
Received 30 December 2021
Revised 23 August 2022
Accepted 29 September 2022
Available online 16 February 2023

Keywords:
Additive manufacturing
Molten pool
Model
Deep learning
Learnability

ABSTRACT

Molten pool characteristics have a significant effect on printing quality in laser powder bed fusion (PBF), and quantitative predictions of printing parameters and molten pool dimensions are critical to the intelligent control of the complex processes in PBF. Thus far, bidirectional predictions of printing parameters and molten pool dimensions have been challenging due to the highly nonlinear correlations involved. To address this issue, we integrate an experiment on molten pool characteristics, a mechanistic model, and deep learning to achieve both forward and inverse predictions of key parameters and molten pool characteristics during laser PBF. The experiment provides fundamental data, the mechanistic model significantly augments the dataset, and the multilayer perceptron (MLP) deep learning model predicts the molten pool dimensions and process parameters based on the dataset built from the experiment and the mechanistic model. The results show that bidirectional predictions of the molten pool dimensions and process parameters can be realized, with the highest prediction accuracies approaching 99.9% and mean prediction accuracies of over 90.0%. Moreover, the prediction accuracy of the MLP model is closely related to the characteristics of the dataset—that is, the learnability of the dataset has a crucial impact on the prediction accuracy. The highest prediction accuracy is 97.3% with enhancement of the dataset via the mechanistic model, while the highest prediction accuracy is 68.3% when using only the experimental dataset. The prediction accuracy of the MLP model largely depends on the quality of the dataset as well. The research results demonstrate that bidirectional predictions of complex correlations using MLP are feasible for laser PBF, and offer a novel and useful framework for the determination of process conditions and outcomes for intelligent additive manufacturing.

1. Introduction

Laser powder bed fusion (PBF) is one of the most important additive manufacturing (AM) approaches, involving progressive one-dimensional (1D) to two-dimensional (2D) and three-dimensional (3D) printing processes with molten pools as the basic unit [1]. The molten pool characteristics have an immediate effect on the microstructure and properties of the laser PBF products and thus are critical to the printing quality [2–5]. It is notable that the molten pool characteristics are closely correlated with key process parameters such as the laser power and scanning speed [6,7]. For example, inadequate molten pool dimensions may cause a lack of fusion defect [8–10]. In contrast, an excessively deep molten pool may involve deep keyholing of the gas/metal interface of the liquid metal, which acts as a potential source of large spherical pores that can be trapped during fast solidification [2]. Thus, quantitative prediction of the correlations between molten pool characteristics and process parameters would be a strong support for the intelligent management of the PBF printing processes and would further the precise control of printing quality [11,12].

Forward and inverse predictions between laser PBF input variables and outcomes are an important theme [13], where process conditions and printing results are critical factors in the comprehension and control of the printing processes [1]. For forward prediction, the targeted molten pool dimensions must be predicted using the process parameters as the input. In contrast, the required process parameters must be predicted using specific molten pool dimensions as the input for inverse prediction. These bidirectional

* Corresponding authors.
E-mail addresses: hlwei@njust.edu.cn (H. Wei), cnwho@mail.njust.edu.cn (W. Liao).

https://doi.org/10.1016/j.eng.2022.09.015

predictions can be a powerful tool for the smart control of printing factors in order to obtain the desired microstructure and mechanical properties of the PBF products [14]. Although forward prediction using MLP has been reported for metal arc welding [15,16], laser PBF [17], and directed energy deposition (DED) [18,19], inverse prediction for desired AM process conditions is still lacking [20,21].

As a data-driven method, deep learning can be used for AM data predictions without the need to explicitly understand the complex mechanisms [22–24]. A multilayer perceptron (MLP) can be an effective tool for the prediction of geometrical features and printing parameters for AM [25,26]. For example, an artificial neural network was used to evaluate the process parameters of the AA2024 alloy deposit during laser DED [18]. MLP was used to predict the geometrical features of laser PBF processes with various laser powers and scanning speeds, and an overall accuracy of up to 90% was obtained for an unseen dataset [17]. Deep learning models can also be used to obtain molten pool characteristics using process monitoring data [27–30]. For example, Schmid et al. [31] proposed a method to automatically measure the molten pool dimensions in the cross-sections of the components. Unsupervised deep learning was utilized to distinguish among the images of molten pools obtained by a high-speed camera [32]. Inverse prediction was successfully carried out using a genetic algorithm (GA) to obtain combinations of arc current, voltage, and scanning speed for a target weld geometry [33]. However, applying GA is time consuming [33,34], and the success of GA is highly dependent upon selection and mutation criteria [35]. In contrast, MLP can provide fast predictions and has a strong ability to map nonlinear relationships among a large volume of data [35]. In brief, deep learning models can be used for the accurate prediction of complex correlations and the efficient processing of AM data, and are beneficial for process optimization and *in situ* smart control [36]. It should be noted that the data-driven nature of MLP requires both adequate volume and adequate quality of the dataset for model training [13,20]. Thus, sufficient experimental and modeling data should be prepared for the high-quality training of the deep learning model [37].

Multiple physical processes occur in a molten pool, such as the fast heating and cooling processes of the feedstock materials; the drastic flow of the liquid metal in the molten pool driven by forces including the surface tension, the Marangoni stress, and the recoil pressure and gravity; and the rapid solidification of the molten pool metal [2,38,39]. These physical processes generate molten pools with variable geometries and dimensions under different printing conditions [40], which exhibit highly nonlinear correlations. The determination of molten pool dimensions is commonly done through experiments and characterizations. However, trial-and-error attempts are often time consuming and expensive, and produce a limited volume of data. In such cases, prediction of the laser PBF input variables and outcomes using deep learning models would be less accurate due to insufficient data for model training.

High-fidelity mechanistic models can help to augment the dataset with appropriate validations against typical experimental results [40,41]. Large-volume and high-quality source data for the training of deep learning models can be constructed using a hybrid experimental and computational approach. Moreover, it is challenging to experimentally observe the spatiotemporal variations of a molten pool and the factors involved including heat transfer and liquid metal flow, which leads to inadequate mechanistic understanding of the complex printing processes. In contrast, multi-physics numerical models can help to reveal the spatiotemporal variations of critical printing factors, such as the evolution of the molten pool and the resultant build [2,6,24,42]. In this way, a better understanding of the mechanisms of experimental phenomena can be achieved, which aids in the analysis of the learnability of certain datasets and the prediction performance of the deep learning models. In addition, virtual printing can be cost effective and provides more design flexibility for typical cases.

However, mechanistic models also present the challenge of inverse prediction from the molten pool data to the process parameter data [2]. To this end, deep learning models such as MLP can be a potential powerful approach for bidirectional prediction for PBF printing. Upon inverse prediction, the desired dimensions of the molten pool can be obtained via the predicted process parameters, which can be useful for the control of printing defects. In brief, the three major modules discussed above—that is, the deep learning model, the laser PBF experiment, and the mechanistic model—should be combined to form a platform for the prediction and understanding of critical process conditions and molten pool characteristics in order to overcome their individual limitations [2,6,43].

To the best of our knowledge, a systematic approach to combine the deep learning model, the laser PBF experiment, and the mechanistic model such as the one proposed here is still lacking in the literature. Under the proposed novel framework, the laser PBF experiment provides fundamental data that can be used to validate the mechanistic model and train the deep learning model. The mechanistic model helps to augment the dataset for the training of the deep learning model. The physics-informed deep learning model is used for both forward and inverse predictions between the process parameters and the molten pool dimensions. This research provides immediate support for the determination of process conditions for desired molten pool characteristics and thus offers a novel and useful component to promote the development of intelligent AM.

2. Methodologies

2.1. Laser PBF experiment

In this work, AA2024 powders produced from the bulk alloy via vacuum induction gas atomization were used for the laser PBF feedstock materials. The particle size range was approximately 20–95 μm in diameter. The powders were dried in an oven at 60 °C for 4 h to remove potential residual moisture and ensure the flowability of the powders. A powder layer thickness of 50 μm was used for all cases. The equipment used in this experiment was a Concept Laser M2 using an ytterbium (Yb)-fiber laser with a radius of 40 μm. The nominal laser power was 400 W, and the wavelength range was 1064–1100 nm. An argon protection environment was used to keep the oxygen content below 0.1% during the process. More experimental details are available in our previous articles [7,44].

Single-track samples were printed by means of laser PBF using various laser powers and scanning speeds; the process parameters are shown in Table 1. The dependences of the molten pool characteristics on laser power or scanning speed were examined via groups of single-variable experimental cases. In addition, the linear energy density—that is, laser power over scanning speed—was utilized to assess the sensitivity of the prediction accuracies of the MLP models. In the experiments, square contours were printed to obtain four single tracks for each identical set of process parameters. The track dimensions of the square contour samples were measured, and the mean values were taken as the experimental results for the validation of the mechanistic model.

2.2. Mechanistic model for laser PBF

In order to compute the complex transport phenomena that occur during laser PBF, conservation equations of mass, momentum, and energy were solved concurrently with the volume of fluid

(VOF) equation in a phenomenological model developed based on OpenFOAM [8]. The details of the model are available in our previous articles [8,38,39]. The spatiotemporal variations of the geometrical features of the molten pools and tracks are computed and demonstrated in the present study. Since the molten pool experiences a significant transient process during linear scanning with constant process parameters, the dimensions of the molten pools were determined after the printing reached a quasi-steady state [38]. The length, width, and height of the computational domain were 1000 μm × 400 μm × 500 μm, and the thickness of the powder layer was 50 μm. The thermophysical properties of the feedstock materials are presented in Table 2 [7].

The laser power range was 100–350 W with an interval of 25 W, and the scanning speed was 300–1500 mm·s^{-1} with an interval of 150 mm·s^{-1}. The two groups of process parameters were combined to obtain 99 groups of data, with the corresponding parameters listed in Table 3. It should be noted that the selected process parameters are within the limits of experimental processing parameters to prevent unpredictable conditions. In order to avoid unbalanced interference for the training of the deep learning model, the 12 computational cases shown in Table 3 that have proximate process parameters with the experimental cases were removed; thus, 87 groups of parameters were left. Such a data volume is adequate for the bidirectional prediction of process parameters and molten pool dimension, supported by a preliminary testing of the data volume sensitivity for the prediction accuracy of the deep learning model.

Table 1
Process parameters used for the laser PBF experiment.

Sample No.	Laser power (W)	Scanning speed (mm·s^{-1})
1	220	300
2	270	300
3	300	300
4	220	600
5	270	600
6	300	600
7	350	600
8	220	900
9	270	900
10	300	900
11	350	900
12	220	1100
13	270	1100
14	300	1100
15	350	1100
16	220	1500

Table 2
Thermophysical properties of AA2024 used in the calculations [7].

Property	Value
Solidus temperature (K)	811
Liquidus temperature (K)	905
Evaporation temperature (K)	2743
Density of metal (kg·m^{-3})	2780
Thermal conductivity of liquid metal (W·m^{-1}·K^{-1})	85.5
Thermal conductivity of solid metal (W·m^{-1}·K^{-1})	188
Specific heat of liquid metal (J·kg^{-1}·K^{-1})	1140
Specific heat of solid metal (J·kg^{-1}·K^{-1})	$768.8 + 0.3T - 2 \times 10^{-4}T^2$
Viscosity of liquid metal (Pa·s)	0.0015
Temperature coefficient of surface tension (N·m^{-1}·K^{-1})	-0.155×10^{-3}
Gas constant (J·K^{-1}·mol^{-1})	8.314
Stefan–Boltzmann constant (W·m^{-2}·K^{-4})	5.67×10^{-8}
Latent heat of fusion (J·kg^{-1})	2.97×10^{5}
Latent heat of evaporation (J·kg^{-1})	1.12×10^{5}

T: temperature.

The mechanistic model was validated by comparing the computational results with the corresponding experimental data. A comparison of molten pool widths under different process parameters is shown in Fig. 1(a), presenting an average error within 4%. Fig. 1(b) depicts the detailed correlations between the molten pool width and the process parameters for both the experimental and computational results. The molten pool depth is shown in Fig. 1(c). The average error of the depth data is 8.98% for the results obtained from the experiments and the mechanistic models. The relatively larger error for the track depth modeling results may originate from the significant fluctuations of the keyhole and thus of the molten pool depth during printing, which will be explored in the subsequent section. Fig. 1(d) shows the transverse sections of the molten pool under different process parameters. With the support of the experimental and mechanistic modeling data, an adequate dataset was built for the subsequent training of the deep learning model. Apart from augmenting the dataset, the mechanistic model helps to uncover the underlying reasons for various prediction accuracies of the MLP model by revealing the spatiotemporal variations of the molten pools and the tracks [8].

2.3. Deep learning model for bidirectional prediction

2.3.1. Forward and inverse predictions

The MLP deep learning model was used to predict the bidirectional correlations between the process parameters and the molten pool dimensions, according to the illustration presented in Fig. 2. For the forward prediction, the molten pool dimensions were predicted via the MLP model using the process parameters as the input. For the inverse prediction, the process parameters were predicted using specific molten pool dimensions as a prerequisite.

The inverse prediction can be further divided into two schemes, as shown in Fig. 3. In Scheme 1, the MLP model input is the molten pool dimensions, while the output is the laser power or scanning speed. In Scheme 2, the MLP model input combines the molten pool dimensions and one process parameter, while the output is another process parameter. For example, the prediction of laser power requires the input of the molten pool width, depth, and scanning speed. Scheme 2 was proposed considering that the same molten pool dimensions may be obtained through the combination of different laser powers and scanning speeds.

According to the prediction results of the inverse MLP models under these two schemes, Scheme 1 and Scheme 2 were selected to predict the process parameters. To ensure the correspondence of the forward and inverse prediction results, the dataset and the MLP model parameters used in the two schemes were consistent. It should be noted that a finite number of cases was carried out within a specific timeframe for both the experiments and the mechanistic models. However, well-trained MLP models possess the capability of providing high-quality meshless results—that is, any arbitrary input can be addressed efficiently to yield a corresponding output for both the forward and inverse predictions.

2.3.2. Dataset allocation

The source data of the process parameters and the molten pool dimensions are the basis of the deep learning training for the MLP model, and the allocation of the dataset affects the resultant prediction performance [45]. The dataset used in this research was composed of 103 sets of process parameters and molten pool dimensions from both the experiment and mechanistic model, which included 16 sets of experimental data and 87 sets of mechanistic modeling data. The dataset was divided into three portions, as presented in Table 4. The training, validation, and independent test datasets were distributed in a ratio of 70:20:13.

Table 3
Process parameters used for the mechanistic model of laser PBF.

Scanning speed (mm·s^{-1})	Laser power (W)										
	100	125	150	175	200	225	250	275	300	325	350
300	S_1	S_2	S_3	S_4	S_5	**S_6**	S_7	S_8	**S_9**	S_{10}	S_{11}
450	S_{12}	S_{13}	S_{14}	S_{15}	S_{16}	S_{17}	S_{18}	S_{19}	S_{20}	S_{21}	S_{22}
600	S_{23}	S_{24}	S_{25}	S_{26}	S_{27}	**S_{28}**	S_{29}	S_{30}	**S_{31}**	S_{32}	**S_{33}**
750	S_{34}	S_{35}	S_{36}	S_{37}	S_{38}	S_{39}	S_{40}	S_{41}	S_{42}	S_{43}	S_{44}
900	S_{45}	S_{46}	S_{47}	S_{48}	S_{49}	**S_{50}**	S_{51}	S_{52}	**S_{53}**	S_{54}	**S_{55}**
1050	S_{56}	S_{57}	S_{58}	S_{59}	S_{60}	S_{61}	S_{62}	**S_{63}**	**S_{64}**	S_{65}	**S_{66}**
1200	S_{67}	S_{68}	S_{69}	S_{70}	S_{71}	S_{72}	S_{73}	S_{74}	S_{75}	S_{76}	S_{77}
1350	S_{78}	S_{79}	S_{80}	S_{81}	S_{82}	S_{83}	S_{84}	S_{85}	S_{86}	S_{87}	S_{88}
1500	S_{89}	S_{90}	S_{91}	S_{92}	S_{93}	**S_{94}**	S_{95}	S_{96}	S_{97}	S_{98}	S_{99}

Bold font refers to the mechanistic model data deleted for MLP model training.
S: Sample.

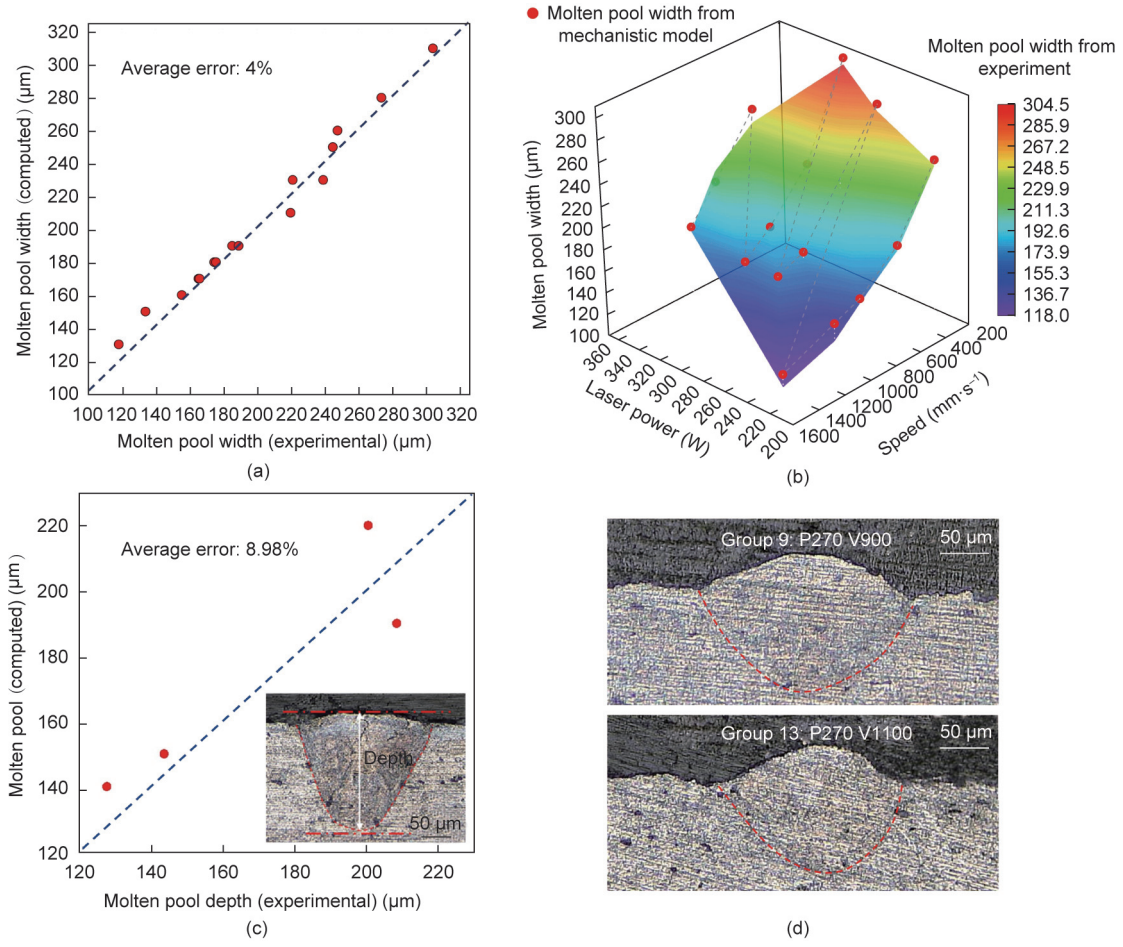

Fig. 1. Validation of the mechanistic model. (a) Comparison of molten pool widths under different process parameters obtained by the experiment and the mechanistic model; (b) molten pool widths obtained by the experiment and the mechanistic model under specific process parameters (the color diagram is based on the data of 16 groups of experimental cases, and the red dots are the molten pool widths obtained by the mechanistic model); (c) comparison of molten pool depths under different process parameters obtained by the experiment and the mechanistic model; (d) transverse sections of the AA2024 samples printed by laser PBF.

Among the three datasets, the training dataset was used to train the MLP model, and the validation dataset was used to check the prediction accuracy of the MLP model during the iterative optimization processes. It should be noted that both the training and validation datasets were used repeatedly during the optimization processes. In contrast, the independent test dataset was reserved beforehand and was only used to examine the prediction accuracy of the optimal MLP model in the final application stage.

In order to avoid potential data accumulation and a resultant prediction bias for the MLP model, close laser powers and scanning speeds were scattered evenly into the three datasets. In addition, all data were normalized before being imported into the MLP model, considering the varieties in the dimensions, values of process parameters, and molten pool dimensions [46]. Thus, the input data were concentrated in the range of 0–1, and the standard deviation was 1. The specific operation can be expressed as follows

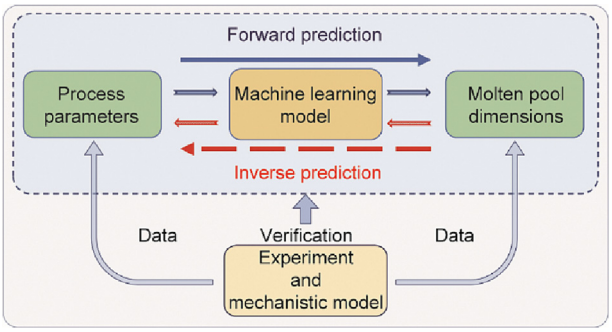

Fig. 2. Schematic diagram of the forward and inverse predictions using MLP, supported by data from the experiment and the mechanistic model.

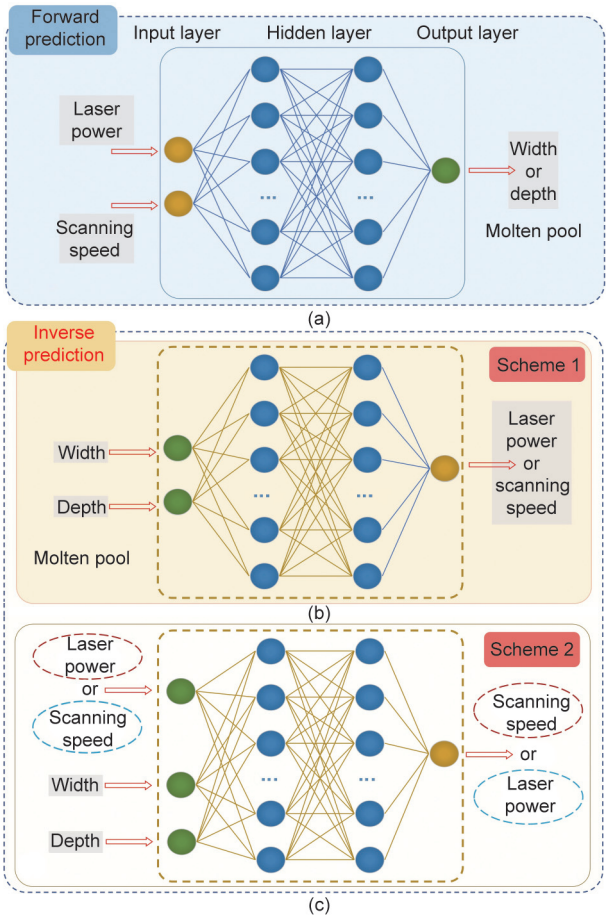

Fig. 3. Illustration of the bidirectional predictions. (a) Forward prediction from process parameters to molten pool dimensions; (b) Scheme 1 of the inverse prediction, from molten pool dimensions to process parameters; (c) Scheme 2 of the inverse prediction, where the input has three variables (i.e., one process variable and two molten pool dimensions).

$$\hat{x}_i = \frac{x_i - E[x_i]}{\sqrt{\mathrm{Var}[x_i]}} \tag{1}$$

where $\hat{x}_i$ is the normalized data; x_i is the original data, $E[x_i]$ is the average value of the dataset, $\sqrt{\mathrm{Var}[x_i]}$ is the standard deviation of the dataset, and i is the order of the data.

2.3.3. MLP model

For the deep learning model, the MLP algorithm was implemented using Python 3.7 with the TensorFlow and Keras modules [47]. The weight and bias of the MLP model were initialized by the Keras internal random initialization method. The rectified linear unit (ReLU) function—one of the most commonly used activation functions of regression neural networks—was applied in this work to avoid the vanishing gradient problem from the logical function (Sigmoid) and hyperbolic tangent function (Tanh) [48].

The prediction performance of the MLP model mainly depends on three factors: the selection of sample features for the training of the neural network [49], the optimization algorithm of the neural network, and the determination of hidden layers and neurons. In this study, the sample features were naturally the process parameters and molten pool dimensions. Among the common optimization algorithms, which include root mean square prop (RMSprop), stochastic gradient descent (SGD), adaptive gradient (AdaGrad), and adaptive moment estimation (Adam) [50], RMSprop was used in the current research, as it can meet the optimization prerequisite of the MLP model. For the selection of hidden layers and neurons, a number of combinations were proposed and examined, with the parameters shown in Tables 5 and 6. By gradually adding neural nodes and hidden layers, the performance of the machine learning model was improved until the optimal performance was obtained [51]. The optimization route of the MLP deep learning model is illustrated in Fig. 4. The learnability of a specific dataset for the MLP model can be assessed through the prediction performance.

In the training process of the MLP models, the K-fold cross-validation method was used to assess the overfitting and selection bias [48], where the K value was 5. The prediction results of the MLP must be analyzed during the training process to provide feedback for the subsequent optimization procedures. The mean squared error (MSE) loss function is commonly used for regression prediction, but it is difficult to intuitively obtain the degree of deviation of the error from the actual value from the MSE value. Therefore, the absolute percentage error (APE) and accuracy rate (AR) were used in this work to represent the model prediction performance; these can be expressed as Eqs. (2) and (3). The goodness of fit index (R2) was also discussed. R2 is determined by Eq. (4).

$$\mathrm{APE} = \frac{|(\hat{y}_i - y_i)|}{y_i} \times 100\% \tag{2}$$

$$\mathrm{AR} = (1 - \mathrm{APE}) \tag{3}$$

$$\mathrm{R2} = 1 - \frac{\sum_i (\hat{y}_i - y_i)^2}{\sum_i (\bar{y}_i - y_i)^2} \tag{4}$$

Table 4
Compositions of different datasets.

Dataset	Amount of data
Training dataset	70 groups (7:63)
Validation dataset	20 groups (4:16)
Independent test dataset	13 groups (5:8)

The numbers in the brackets refer to the data obtained via the experiment and the mechanistic model, respectively.

Table 5
Neuron numbers for the MLP models with a single hidden layer.

Model number	Neurons of the hidden layers
Model 1	10
Model 2	32
Model 3	48
Model 4	64
Model 5	80

Table 6
Neuron numbers for the MLP models with multiple hidden layers.

Model number	The number of neurons in the hidden layer				
	First layer	Second layer	Third layer	Forth layer	Fifth layer
Model 6	48	32	—	—	—
Model 7	48	32	16	—	—
Model 8	64	48	32	16	—
Model 9	64	48	32	16	8

where $\hat{y}_i$ indicates the predicted value of the MLP; y_i is the actual value; and $\bar{y}_i$ is the mean value.

3. Results and discussion

This section first presents the optimization of the deep learning MLP models for both forward and inverse predictions, considering different numbers of hidden layers and neurons. Subsequently, the application of the optimal MLP models under two typical conditions—that is, using the reserved source data and exterior fresh data—is examined. Finally, the learnability of various data and the mechanisms for various prediction accuracies of the MLP models are assessed.

3.1. Optimization of the deep learning model

3.1.1. Forward prediction

Fig. 5 shows the prediction results of molten pool width and depth during the optimization process of the MLP models. The training and validation datasets presented in Table 4 were used for the optimization. The parameters of the MLP models are shown in Tables 5 and 6. The prediction ARs in Fig. 5 are calculated by Eq. (3). Fig. 5(a) shows the prediction results of molten pool width using a single hidden layer with different neurons, referring to Models 1–5. In these cases, the mean prediction ARs of the molten pool widths increased with the neuron number. Models 6–9 show that the mean prediction ARs of the molten pool widths were approximately 95% and exhibited a weak dependency on the number of hidden layers. The highest prediction accuracy was close to 100% and the lowest accuracy was above 80% for all cases shown in Fig. 5(a). Considering the lowest and mean prediction accuracies, the optimal MLP model for the molten pool width prediction was determined to be Model 6.

Fig. 5(b) shows that the lowest prediction accuracy of molten pool depth increased initially but then decreased with the number of neurons, with the same trend occurring for hidden layers. The highest prediction accuracy was 100%, and the lowest was 80%. Overall, the optimal MLP model for molten pool depth prediction was Model 8. The mean and the lowest prediction accuracies presented in Figs. 5(a) and (b) imply that the predictions of molten pool width were more accurate than those of molten pool depth. The underlying mechanism will be explored in Section 3.3.

3.1.2. Inverse prediction

Fig. 6 depicts the results of two inverse prediction schemes for laser power and scanning speed with different MLP models. The data used were the training and validation datasets presented in Table 4, and the APEs were calculated by Eq. (2). It can be seen from Fig. 6 that, regardless of the laser power or scanning speed, the prediction errors of Scheme 1 are generally higher than those of Scheme 2. Comparing the prediction results using Scheme 1 and Scheme 2, it can be inferred that the dependences of the process parameters must be considered during the inverse prediction. Therefore, the inverse prediction approach refers to Scheme 2 in subsequent sections.

Fig. 7 illustrates the variations in prediction accuracies with different MLP models for the inverse prediction of process parameters, corresponding to Scheme 2 in Fig. 6. In the figure, the prediction accuracies of Models 1–5 are shown using a single hidden layer with different neurons for laser power and scanning speed, respectively. In these cases, the mean prediction accuracies of the laser power and scanning speed both increased with the number of neurons. For Models 6–9, the prediction results for laser power and scanning speed are shown using different numbers of hidden layers. It can be observed from Fig. 7(b) that the lowest prediction accuracy for scanning speed increased with the number of hidden layers for Models 6 and 7. This accuracy decreased for Models 8 and 9, however, which may result from overfitting of the laser PBF data.

As illustrated in Fig. 7, the mean prediction accuracies for laser power and scanning speed are both approximately 90%. In general, the prediction of laser power is more accurate than that of scanning speed. Among the nine groups of MLP models in Fig. 7(a), the highest prediction accuracy for laser power is 99.9% and the lowest is 41.0%. Considering the lowest and mean accuracies, the optimal model for laser power prediction is Model 8. The highest prediction accuracy for scanning speed is 99.9% and the lowest is 17.0%, as shown in Fig. 7(b). Considering the lowest and mean accuracies of the nine MLP models, the optimal model for scanning speed prediction is Model 8.

3.2. Applications of the deep learning model

3.2.1. Forward prediction

After optimization using the training and validation datasets, the performance of the MLP models in the prediction for the originally reserved and exterior datasets is examined in this section. As listed in Table 7, the reserved dataset—that is, the independent test dataset—came from the source data composed of the experimental and mechanistic modeling results presented in Table 4. The exterior dataset was generated via interpolation and extrapolation of the source dataset presented in Table 4. The interpolation dataset was constructed considering the same range of process parameters as the training and validation datasets, but without identical values against the source data. In contrast, the extrapolation dataset was constructed beyond the range of the process parameters of the source data.

(1) **Prediction for the independent test dataset.** The performance of the optimal MLP model was first examined through the forward prediction of the molten pool dimensions using laser PBF cases in the independent test dataset. Figs. 8(a) and (b) present comparisons of the targeted and predicted molten pool widths. The targeted molten pool widths are the source data from the experimental and mechanistic modeling results, while the predicted widths are from the MLP model for identical process parameters. Both the data points and the rendered color graphs demonstrate approximate values of the targeted and predicted results. The prediction accuracies are further presented in Fig. 8(c). It can be observed that the highest prediction accuracy for molten pool width is close to 100.0%; the mean is 96.6%, and the

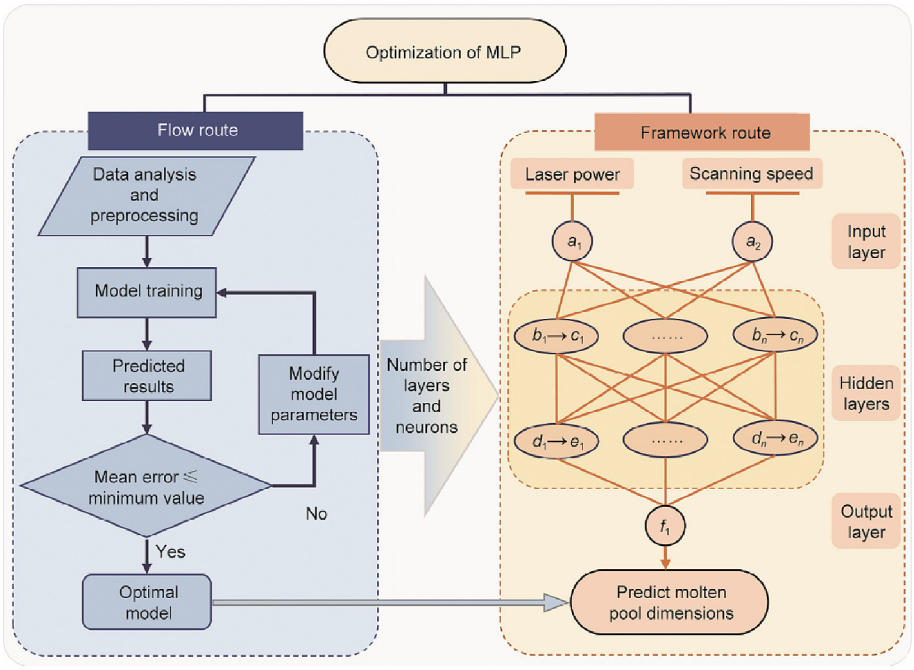

Fig. 4. Optimization of the MLP deep learning model. a_1, a_2: input; b_1, b_n, d_1, d_n: input values received by each neuron in the hidden layer from previous layers; c_1, c_n, e_1, e_n: the output of different neurons processed by the activation function in the hidden layer; f_1: the final output.

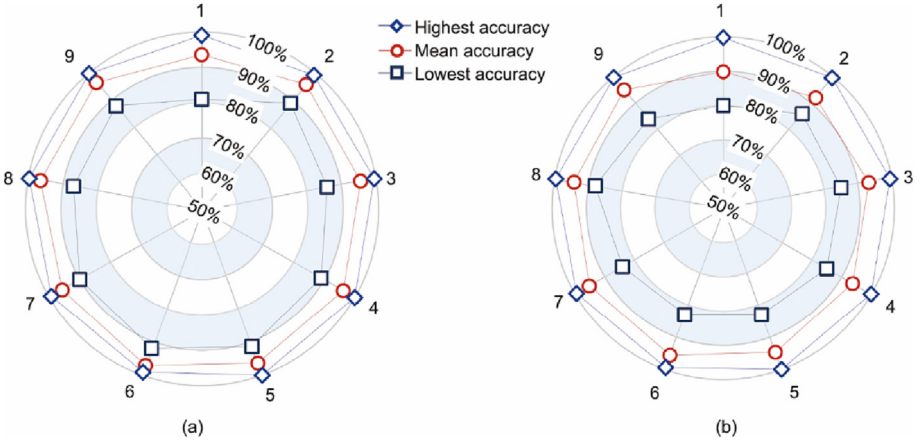

Fig. 5. Prediction accuracies of the molten pool dimensions using different MLP deep learning models. (a) Molten pool width; (b) molten pool depth. The numbers 1–9 refer to the MLP models presented in Tables 5 and 6. The data used include the training dataset and the validation dataset in Table 4. The presented accuracies were obtained via the validation dataset.

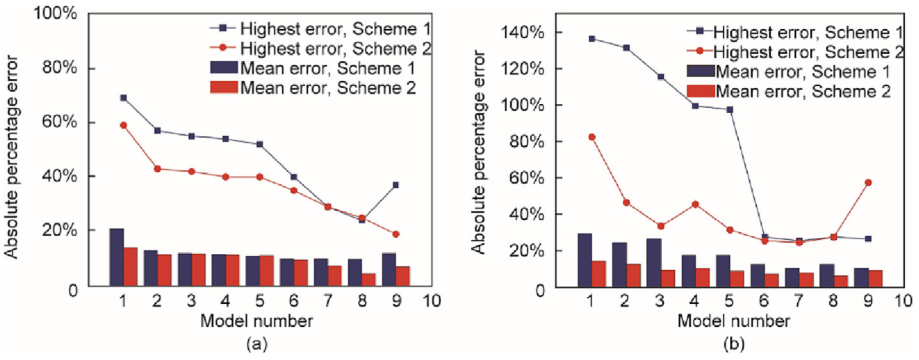

Fig. 6. Prediction errors of the two inverse prediction schemes using different MLP deep learning models. (a) Laser power as the prediction output; (b) scanning speed as the prediction output. The model number refers to the MLP models presented in Tables 5 and 6.

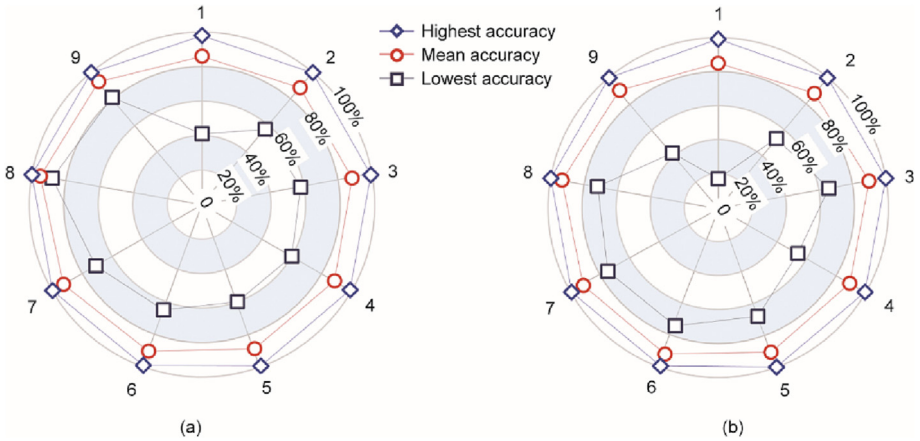

Fig. 7. Prediction accuracies of process parameters with different MLP deep learning models. (a) Laser power as the prediction output; (b) scanning speed as the prediction output.

lowest is higher than 90.0%. The calculated R2 value is correspondingly 0.97.

Figs. 9(a) and (b) show the targeted and predicted molten pool depths under the same process parameters for the independent test dataset. Both the data points and the rendered color distributions are close, as shown in Figs. 9(a) and (b), indicating a decent agreement of the predicted results using the MLP model with the source data. In addition, Fig. 9(c) shows the highest prediction accuracy of 98.4% and the lowest accuracy of 89.0%, corresponding to the fifth and the twelfth cases, respectively. The mean prediction accuracy for the molten pool depth is 94.5%, and the R2 value is 0.97. Thus, all cases with the independent test dataset indicate the high prediction accuracy of the MLP model for the reserved laser PBF cases.

(2) **Prediction for the interpolation and extrapolation datasets.** In addition to applying the MLP model to cases with reserved source data, the MLP model was further examined using various laser PBF cases with interpolation and extrapolation data. The former was done to assess the performance of the MLP models for process parameters within the same range of the source data, and the latter was done to test the applicability of the MLP model for conditions beyond the range of the source data. The prediction results of molten pool width under the process parameters from interpolation and extrapolation are shown in Fig. 10. In Figs. 10(a) and (b), the laser powers corresponding to the extrapolated process parameters are between 350–400 W. This range ensures the basic requirements of extrapolation and further prevents errors caused by process parameters beyond the maximum laser power range of the processing equipment. Fig. 10(c) shows that the prediction accuracies for molten pool width are all above 90%, and that the results for the interpolation cases are better than those for the extrapolation cases. This is also illustrated by the R2 values, which are 0.95 and 0.93 for the interpolation and extrapolation cases, respectively. Under the process parameters from extrapolation, the highest, the mean, and the lowest prediction accuracies of the molten pool widths are 98.0%, 97.3%, and 96.6%, respectively.

Fig. 11 shows the prediction results of molten pool depth under the process parameters from interpolation and extrapolation. As shown in Figs. 11(a) and (b), the predicted molten pool depths are close to the target molten pool depths. In Fig. 11(c), the mean prediction accuracy of the molten pool depths for the interpolation cases is 94.66%. The mean prediction accuracy indicates that the depth can be predicted accurately within the same parameter range, even if different intervals are taken. Under the process parameters from extrapolation, the highest accuracy is approximately 100%, and the mean prediction accuracy of the molten pool depths is 95.99%. The R2 values in both cases are 0.95.

Table 7
Application of the MLP model for process parameters from various datasets.

Dataset	Dataset number	Laser power (W)	Scanning speed ($mm \cdot s^{-1}$)
Independent test dataset	1	125	1350
	2	150	600
	3	100	600
	4	325	450
	5	300	750
	6	250	450
	7	200	900
	8	350	1200
	9	220	1100
	10	300	300
	11	270	900
	12	270	300
	13	270	600
Interpolation dataset	14	180	700
	15	130	400
	16	310	800
	17	210	500
	18	330	660
	19	260	430
Extrapolation dataset	20	390	1500
	21	400	1350
	22	375	1200
	23	360	1050
	24	390	900
	25	400	750
	26	375	600
	27	360	450

3.2.2. Inverse prediction

After optimization using the training and validation datasets via the method described in Section 2.3.2, the performance of the MLP models in the inverse predictions for the independent test, interpolation, and extrapolation datasets presented in Table 7 are examined in this section.

(1) **Prediction of laser power.** Fig. 12 shows the prediction results of laser power using three different types of datasets. It should be noted that the model inputs are scanning speeds and the corresponding molten pool widths and depths, while the predicted outputs are laser powers. As shown in Fig. 12(b), when predicting laser power using independent process parameters, the highest prediction accuracy is 99.9% and the lowest is 84.0%,

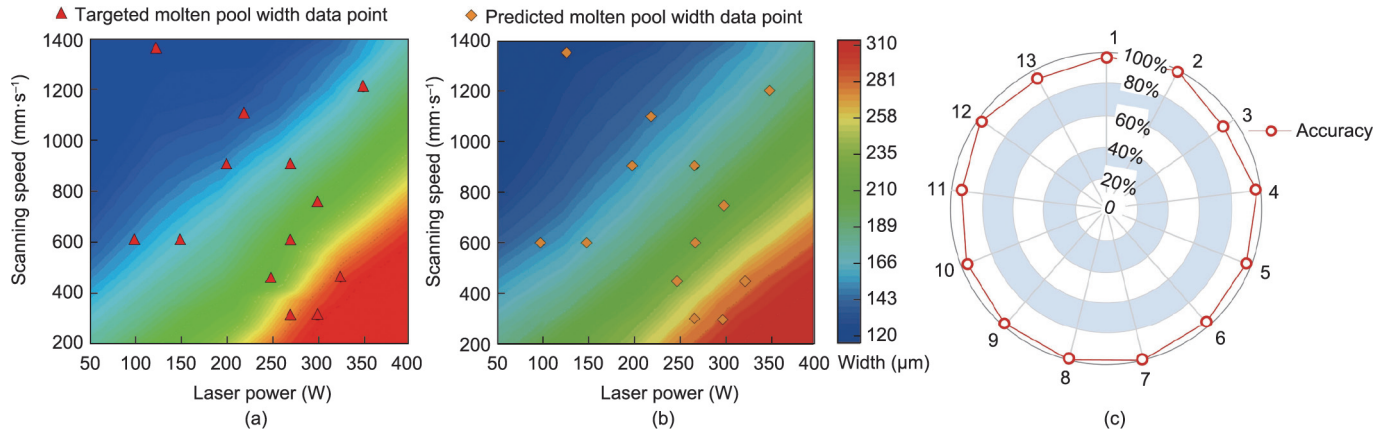

Fig. 8. Prediction results of molten pool width using independent process parameters. (a) Targeted molten pool width; (b) molten pool width predicted by the MLP model; (c) prediction accuracy for all cases in the independent test dataset. The numbers 1–13 refer to the cases of the independent test dataset in Table 7.

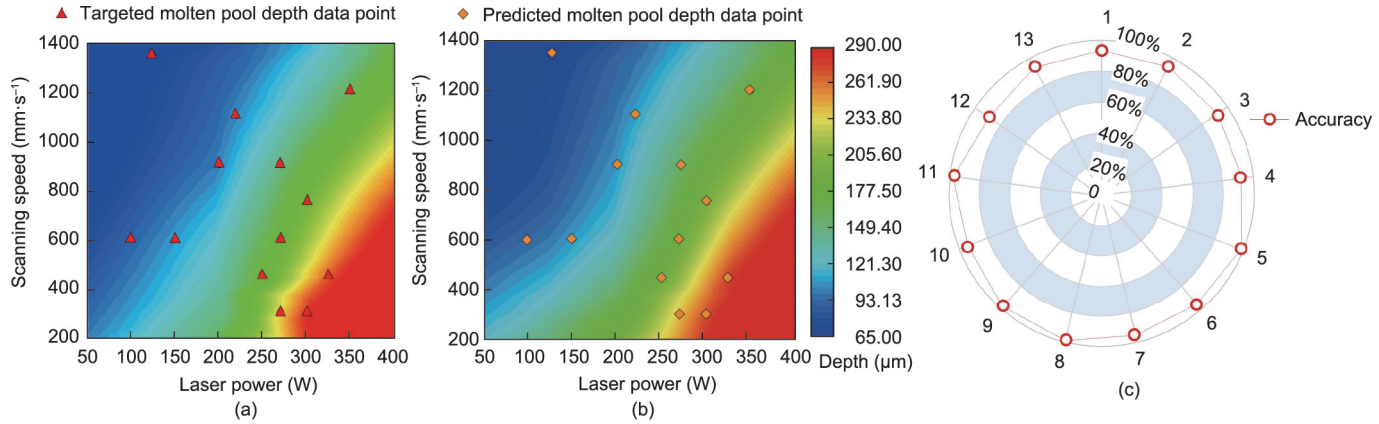

Fig. 9. Prediction results of molten pool depth using independent process parameters. (a) Targeted molten pool depth; (b) molten pool depth predicted by the MLP model; (c) prediction accuracy for all cases in the independent test dataset.

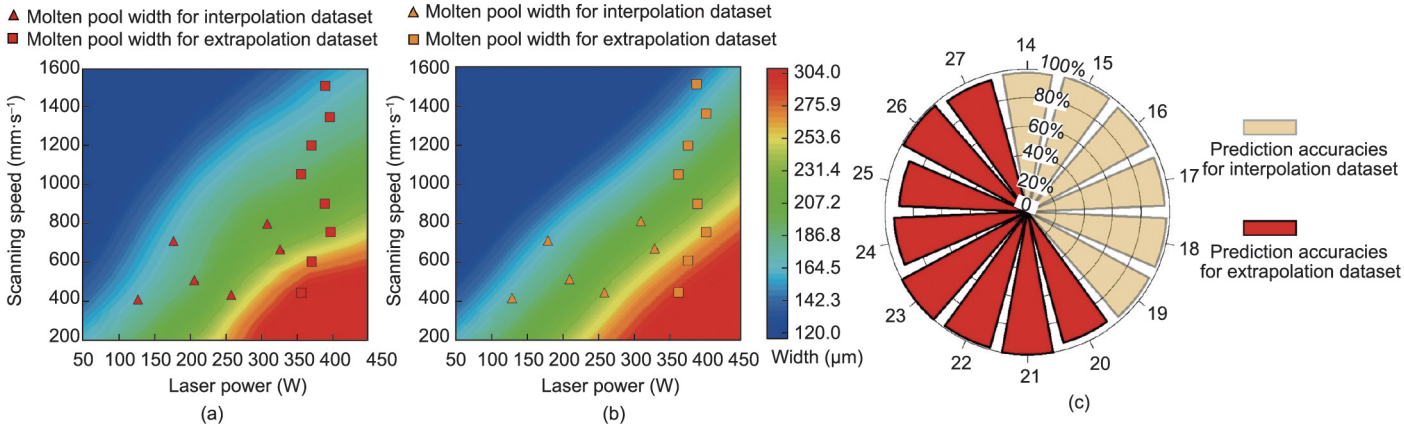

Fig. 10. Prediction results of molten pool width for the interpolation and extrapolation datasets. (a) Targeted molten pool width obtained via the mechanistic model; (b) molten pool width predicted by the MLP model; (c) prediction accuracies for all cases in the interpolation and extrapolation dataset. The numbers 14–27 refer to the interpolation and extrapolation datasets in Table 7.

corresponding to the first and ninth cases, respectively. The corresponding R2 value is 0.96. The mean AR is over 90% for all cases. The prediction results of laser power under the three types of inputs demonstrate the decent accuracy of the well-trained MLP model for inverse predictions.

(2) **Prediction of scanning speed.** Fig. 13 shows the prediction results of scanning speed under three different types of data. It should be noted that the model inputs are laser powers and corresponding molten pool widths and depths, while the predicted outputs are scanning speeds. Fig. 13 shows that the prediction

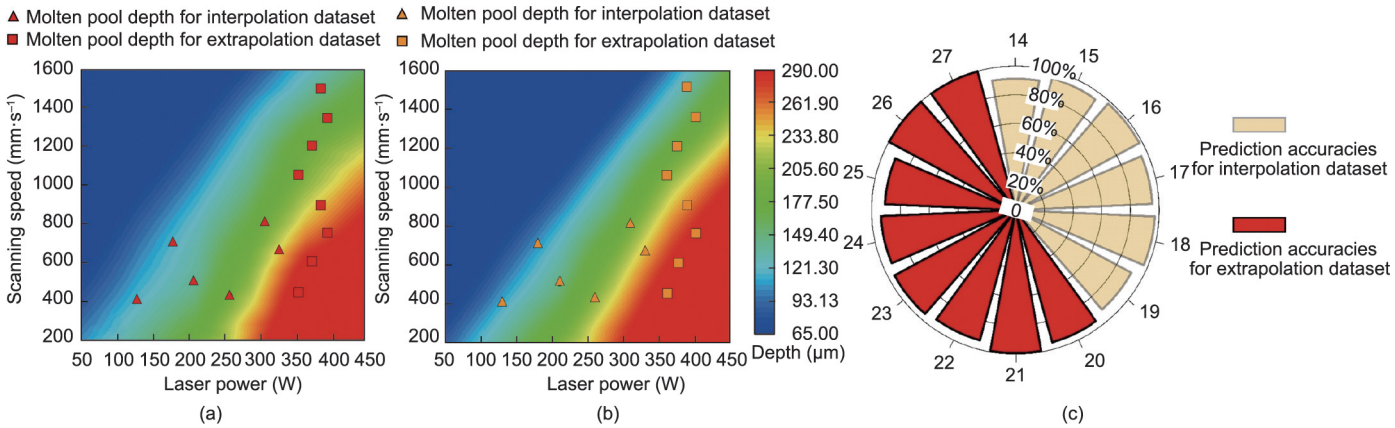

Fig. 11. Prediction results of molten pool depth for the interpolation and extrapolation datasets. (a) Targeted molten pool depth obtained via the mechanistic model; (b) molten pool depth predicted by the MLP model; (c) prediction accuracies for all cases in the interpolation and extrapolation dataset.

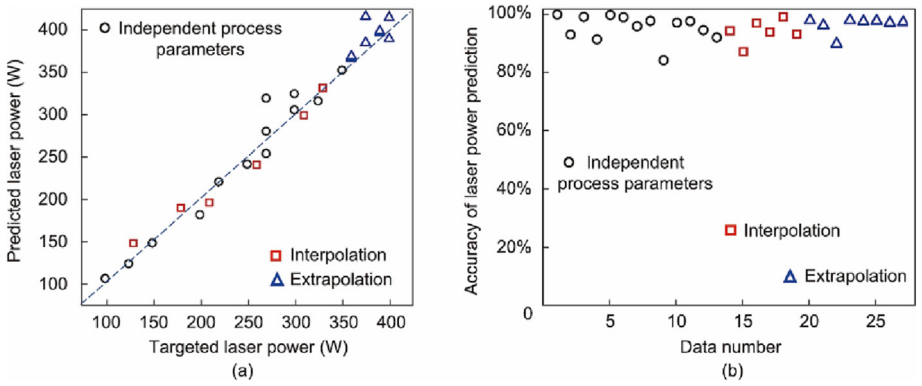

Fig. 12. Predicted laser powers using various datasets presented in Table 7. (a) Targeted and predicted laser powers; (b) prediction accuracies of the MLP model. Model inputs are molten pool widths, depths, and scanning speeds; predicted outputs are laser powers.

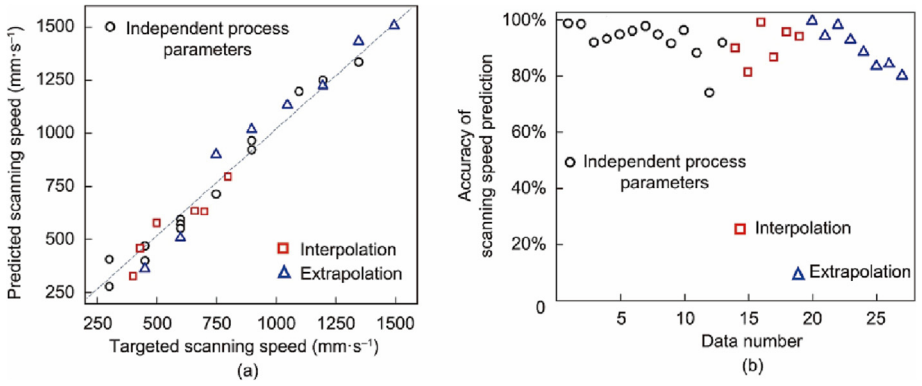

Fig. 13. Predicted scanning speeds using various datasets presented in Table 7. (a) Targeted and predicted scanning speeds; (b) prediction accuracies of the MLP model.

accuracy of scanning speed fluctuates more severely than that of laser power. As evaluated by the mean accuracies, the prediction accuracies for the interpolation and extrapolation cases are lower than those for the independent test cases. The R2 values of the independent test cases, interpolation cases, and extrapolation cases are 0.97, 0.86, and 0.93, respectively. As shown in Fig. 13(b), the highest and the mean prediction accuracies are 98.8% and 93.0% for the independent test dataset, respectively. For the interpolation and extrapolation datasets, the highest prediction accuracy for scanning speed exceeds 99%, and the mean accuracies are 91% and 90%, respectively. It can be observed that the lowest prediction accuracy of scanning speed occurs with a slow scanning speed, corresponding to a high line energy density. The mechanisms behind the low prediction accuracy with a slow scanning speed will be explained in Section 3.3.

In brief, the above results demonstrate the decent prediction accuracy of the proposed model for the process parameters and molten pool dimensions, covering the independent test, interpolation conditions, and extrapolation conditions. These forward and inverse prediction performances demonstrate the

reliable capabilities of the well-trained MLP models for various laser PBF conditions.

3.3. Learnability of the data

As a data-driven approach, the performance of the MLP model largely depends on the characteristics of the dataset. It should be noted that not all data are well-suited for the training and prediction of deep learning models [52]. Although the ability to quickly learn and adapt from a small amount of data is desirable [53], qualified candidates for deep learning models often comprise sufficient data featuring physical meanings or statistical orders. In this section, the learnability of the data—including the volume and the quality of the dataset—is examined for the laser PBF processes.

3.3.1. Dataset volume and prediction accuracies

The volume of the dataset is a critical factor for the training of MLP models, considering the data-driven nature of deep learning. In this subsection, the prediction performances of the MLP models are compared for laser PBF cases using different datasets—namely, one for only the experimental data and the other for the hybrid experimental and mechanistic modeling data. The prediction accuracy of molten pool width is taken as an example for comparison, supported by the identical optimization method used for the MLP models. For the experimental data, the cases listed in Table 1 are used for training, validation, and independent testing. The interpolation and extrapolation datasets listed in Table 7 are further used to verify the actual performance of the trained optimal model. In contrast, the cases listed in Table 4 are used for the hybrid experimental and mechanistic modeling data. The prediction results are presented in Table 8.

As shown in Table 8, the mean prediction accuracies of the molten pool widths are significantly lower when only the experimental data are used. For example, the mean prediction accuracy for the independent test dataset is only 59.0% when pure experimental data are used for the training and validation of the MLP model. In contrast, the mean accuracy is 96.6% when hybrid data are used. Thus, a larger volume of data should be generated for a decent prediction accuracy. Testing cases from 16 to over 100 groups of data were explored during this study, and the volume indicated in Table 4 was determined considering both the prediction accuracy and the preparation efficiency. In brief, it can be concluded that adequate data are a prerequisite for the accurate prediction of the MLP deep learning models for laser PBF, and mechanistic models can serve as a powerful tool for the augmentation of the dataset.

3.3.2. Dataset quality and prediction accuracies

Apart from the volume, the quality of the dataset may also affect the prediction accuracy of the MLP model. Fig. 14(a) shows that the prediction accuracies of the molten pool widths are higher overall than those of the molten pool depths during forward predictions. Moreover, the prediction accuracies of depths decrease when higher energy densities are used. Fig. 14(b) shows the variation of inverse prediction accuracy with linear energy density. It can be observed that the prediction accuracy of scanning speed is significantly lower when a higher linear energy density is used. Fig. 14(c) shows the variation of molten pool dimensions with linear energy density. It can be observed that the variation of the molten pool depths scattered significantly when the linear energy density was over 0.5 J·mm^{-1}. The standard deviations were 67.09 and 49.46 for the molten pool depth and width, respectively. The differences in these deviations originated from the physical nature of the molten pool during laser PBF.

Fig. 15 compares the molten pool and deposited track features obtained under different linear energy densities of laser PBF. The 3D temperature fields and deposit profiles are presented in Figs. 15(a) and (b). It can be observed from Fig. 15(f) that the molten pool depth varies significantly along the scanning direction. In contrast, the bottom of the printed track in Fig. 15(e) fluctuates less when using a linear energy density of 0.2 J·mm^{-1}. Moreover, the variations of the track widths are both trivial, as shown in Figs. 15(c) and (d). These differences may originate from the mechanisms of heat transfer and fluid flow during laser PBF. A deep and volatile

Table 8
Prediction results of molten pool width with different data.

Dataset	Training:validation: independent test	Mean prediction accuracy for independent test dataset	Mean prediction accuracy for interpolation dataset	Mean prediction accuracy for extrapolation dataset
Experimental data	11:3:2	59.0%	48.5%	68.3%
Experimental and modeling data	70:20:13	96.6%	97.3%	96.3%

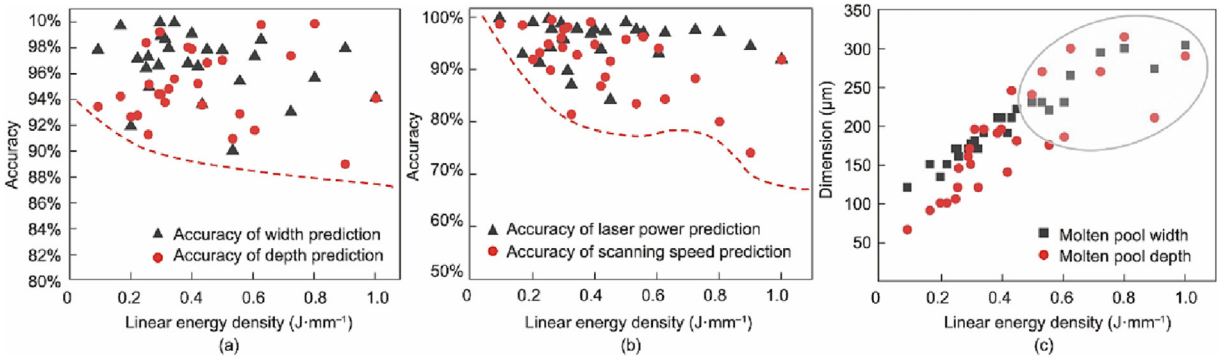

Fig. 14. Variations of prediction accuracies and molten pool dimensions with linear energy density. (a) Forward prediction accuracies for molten pool dimensions; (b) inverse prediction accuracies for process parameters; (c) variations of molten pool dimensions with linear energy density.

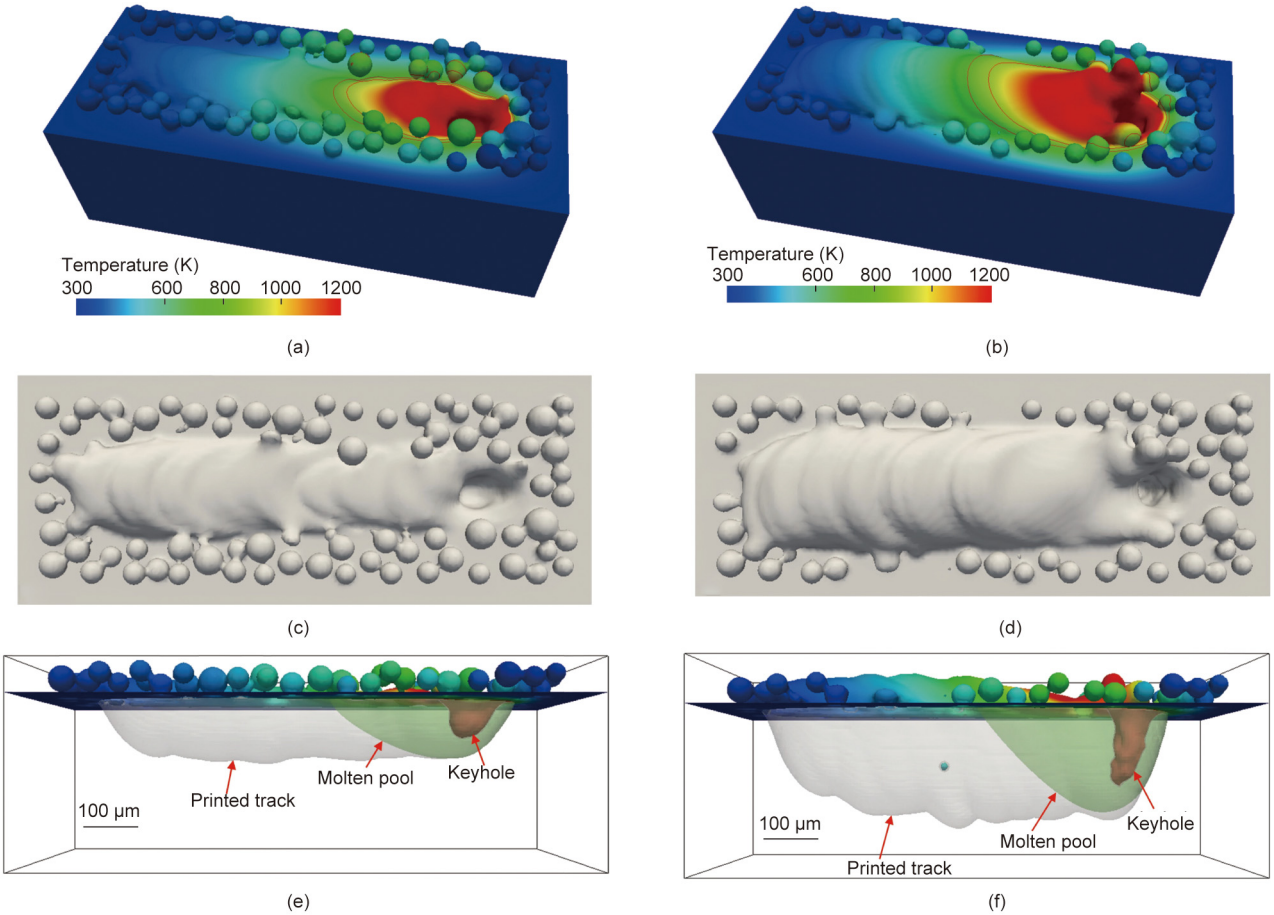

Fig. 15. Molten pool and deposited track features obtained under different process conditions. (a), (c), and (e) 220 W and 1100 mm·s^{-1} with a linear energy density of 0.2 J·mm^{-1}; (b), (d), and (f) 300 W and 600 mm·s^{-1} with a linear energy density of 0.5 J·mm^{-1}. Parts (a) and (b) provide a 3D view of the build, (c) and (d) provide a top view, and (e) and (f) provide a longitudinal view of the printed zone and the molten pool.

keyhole was generated, and the keyhole largely determined the penetration depth of the molten pool during printing [54,55]. It is notable that the shape and size of the keyhole depend on the dramatic flow of the liquid metal and the spatter of powder particles, which would be more severe under high energy density conditions [2,56,57]. The fluctuation of the molten pool depth is greater than that of the width due to the greater sensitivity of the molten pool along the keyhole depth direction. Therefore, the prediction accuracies of the molten pool depths are lower than those of the widths when using the MLP models.

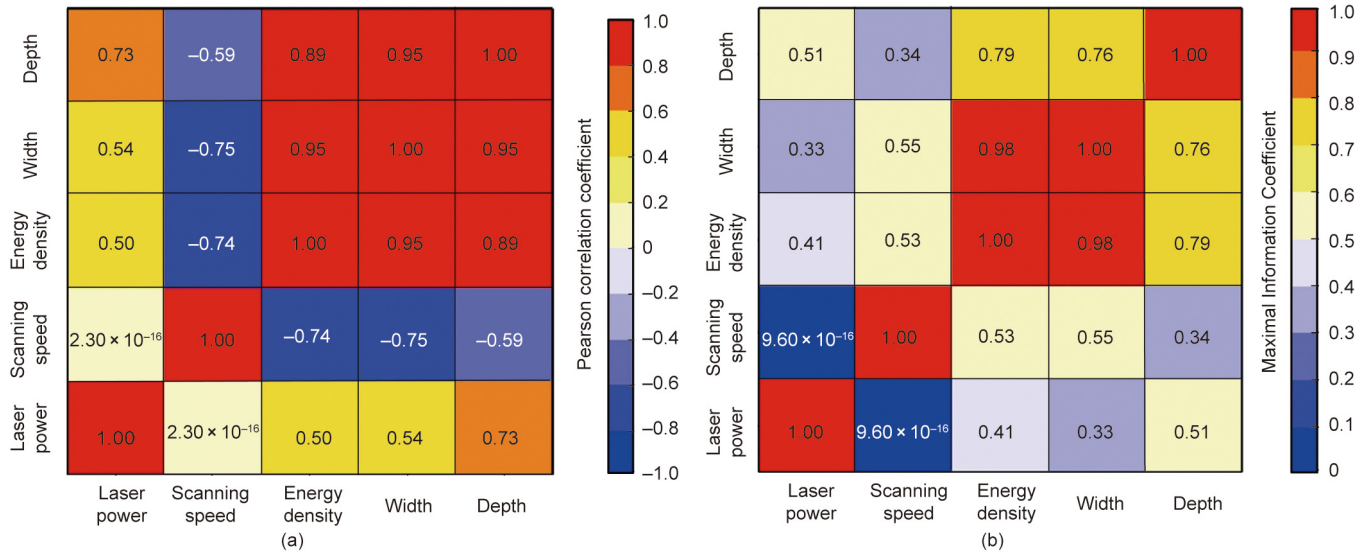

Fig. 16. Correlation analysis of parameters. (a) PCC between parameters; (b) MIC between parameters.

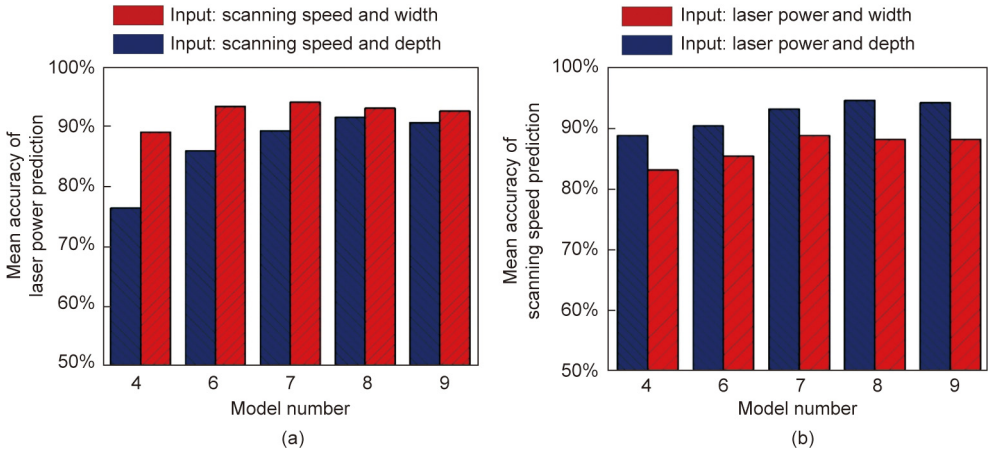

Fig. 17. Variations of the inverse prediction accuracy with different MLP model input variables. (a) Mean prediction accuracy of laser power; (b) mean prediction accuracy of scanning speed.

3.3.3. Dependence assessment for input and output variables

To reveal the correlations between the process parameters and molten pool dimensions, the Pearson correlation coefficient (PCC) and maximal information coefficient (MIC) were used. Data analysis was done for the 99 cases presented in Table 3. The PCC can be used to measure the degree of linear correlation between variables, where the correlation degree is proportional to the absolute values of the coefficients. The MIC can be used for seeking linear or nonlinear correlations between variables [58]. A higher value of the MIC between 0 and 1 indicates a closer correlation. As presented in Fig. 16, scanning speed exhibited a closer correlation with molten pool width, while laser power had a closer correlation with molten pool depth. In addition, the significance level of the correlation analysis between the process parameters and the molten pool dimensions was calculated. It was found that the significance values of the laser power between the width and depth of the molten pool were 6.46×10^{-9} and 1.86×10^{-17}, respectively. The significance values of the scanning speed between the width and depth of the molten pool were 1.78×10^{-19} and 1.84×10^{-10}, respectively. Therefore, the results of the correlation analysis of the process parameters and the molten pool dimensions are significant.

To further explore the correlations between the molten pool dimensions and the process parameters, four new sets of input variables were used, as shown in Fig. 17. Only a single molten pool dimension and a single process parameter were used for the MLP model input. It should be noted that, in Fig. 3, both the molten pool width and depth were used for the input of the MLP model in Schemes 1 and 2 of the inverse prediction. Fig. 17(a) shows that the mean prediction accuracy of the laser powers was higher when the molten pool depths were included in the MLP input. In contrast, Fig. 17(b) shows that the mean prediction accuracy of the scanning speeds was higher when the molten pool widths were included in the MLP input. The comparisons indicate that molten pool depth is more relevant to laser power than molten pool width.

4. Conclusions

The molten pool characteristics have a significant effect on the build quality of laser PBF, given the multidimensional printing works. This research combined an experiment, a high-fidelity mechanistic model, and an MLP deep learning model to carry out the bidirectional prediction of critical process parameters and molten pool characteristics during laser PBF. The dependences of the prediction accuracy on the learnability of the dataset were evaluated. The following conclusions can be drawn from this work:

(1) Both forward and inverse predictions of the molten pool dimensions and key process parameters can be realized for laser PBF, with a prediction accuracy approaching 99.9%. Forward prediction from the laser PBF process parameters—particularly the interpolated and extrapolated values—to molten pool dimensions can help in forecasting molten pool characteristics before experiments, whereas inverse prediction from molten pool dimensions to process parameters is useful when specific molten pool dimensions are desired.

(2) The prediction accuracy of the MLP model is closely related to the volume of the dataset. The highest prediction accuracy was 97.3% with augmentation of the dataset via the mechanistic model. In contrast, the highest prediction accuracy was 68.3% and the lowest was 48.5% when using only the experimental data for MLP model training. Thus, a well-tested mechanistic model can effectively address the issue of insufficient data from experiments.

(3) The prediction accuracy of the MLP model largely depends on the quality of the dataset. For example, it was found that the forward prediction accuracy of the process parameters to the molten pool depth was lower than that for the molten pool width. The reason is that the molten pool depth exhibits poor data regularity due to the complex transient keyhole characteristics.

(4) The parameters of the MLP models are important components of the prediction accuracy. Accurate predictions require an appropriate optimization method, activation function, and hidden layers and neurons.

This study provides an insightful path for explorations of the highly nonlinear correlations in laser PBF. Although the predictions are exemplified through process parameters and molten pool characteristics, the proposed methodologies are expected to be feasible for other conditions requiring forward and inverse predictions of variables with complex interdependences. Moreover, the proposed framework can serve as a critical building block for digital twins of AM, and thus promotes the future development of intelligent AM equipment and processes [2,6,59–61].

Acknowledgments

This work is supported by the Frontier Leading Technology Basic Research Project of Jiangsu (BK20202007), the National Natural Science Foundation of China (52175330), and the Fundamental Research Funds for the Central Universities (30921011202).

Compliance with ethics guidelines

Mingzhi Zhao, Huiliang Wei, Yiming Mao, Changdong Zhang, Tingting Liu, and Wenhe Liao declare that they have no conflict of interest or financial conflicts to disclose.

References

[1] DebRoy T, Wei HL, Zuback JS, Mukherjee T, Elmer JW, Milewski JO, et al. Additive manufacturing of metallic components—process, structure and properties. Prog Mater Sci 2018;92:112–224.
[2] Wei HL, Mukherjee T, Zhang W, Zuback JS, Knapp GL, De A, et al. Mechanistic models for additive manufacturing of metallic components. Prog Mater Sci 2021;116:100703.
[3] Shi R, Khairallah SA, Roehling TT, Heo TW, McKeown JT, Matthews MJ. Microstructural control in metal laser powder bed fusion additive manufacturing using laser beam shaping strategy. Acta Mater 2020;184:284–305.
[4] Wei HL, Knapp GL, Mukherjee T, DebRoy T. Three-dimensional grain growth during multi-layer printing of a nickel-based alloy inconel 718. Addit Manuf 2019;25:448–59.
[5] Wei HL, Elmer JW, DebRoy T. Three-dimensional modeling of grain structure evolution during welding of an aluminum alloy. Acta Mater 2017;126:413–25.
[6] DebRoy T, Mukherjee T, Wei HL, Elmer JW, Milewski JO. Metallurgy, mechanistic models and machine learning in metal printing. Nat Rev Mater 2021;6(1):48–68.
[7] Cao Y, Wei HL, Yang T, Liu TT, Liao WH. Printability assessment with porosity and solidification cracking susceptibilities for a high strength aluminum alloy during laser powder bed fusion. Addit Manuf 2021;46:102103.
[8] Wei HL, Cao Y, Liao WH, Liu TT. Mechanisms on inter-track void formation and phase transformation during laser Powder Bed Fusion of Ti–6Al–4V. Addit Manuf 2020;34:101221.
[9] Mukherjee T, Wei HL, De A, DebRoy T. Heat and fluid flow in additive manufacturing—Part I: modeling of powder bed fusion. Comput Mater Sci 2018;150:304–13.
[10] Mukherjee T, Wei HL, De A, DebRoy T. Heat and fluid flow in additive manufacturing—Part II: powder bed fusion of stainless steel, and titanium, nickel and aluminum base alloys. Comput Mater Sci 2018;150:369–80.
[11] McCann R, Obeidi MA, Hughes C, McCarthy É, Egan DS, Vijayaraghavan RK, et al. *In-situ* sensing, process monitoring and machine control in laser powder bed fusion: a review. Addit Manuf 2021;45:102058.
[12] Yavari R, Riensche A, Tekerek E, Jacquemetton L, Halliday H, Vandever M, et al. Digitally twinned additive manufacturing: detecting flaws in laser powder bed fusion by combining thermal simulations with *in-situ* melt pool sensor data. Mater Des 2021;211:110167.
[13] Karniadakis GE, Kevrekidis IG, Lu L, Perdikaris P, Wang S, Yang L. Physics-informed machine learning. Nat Rev Phys 2021;3(6):422–40.
[14] Liu Q, Wu H, Paul MJ, He P, Peng Z, Gludovatz B, et al. Machine-learning assisted laser powder bed fusion process optimization for AlSi10Mg: new microstructure description indices and fracture mechanisms. Acta Mater 2020;201:316–28.
[15] Xiong J, Zhang G, Hu J, Wu L. Bead geometry prediction for robotic GMAW-based rapid manufacturing through a neural network and a second-order regression analysis. J Intell Manuf 2014;25:157–63.
[16] Nagesh DS, Datta GL. Prediction of weld bead geometry and penetration in shielded metal-arc welding using artificial neural networks. J Mater Process Technol 2002;123(2):303–12.
[17] Le-Hong T, Lin PC, Chen JZ, Pham TDQ, Van Tran X. Data-driven models for predictions of geometric characteristics of bead fabricated by selective laser melting. J Intell Manuf 2021;9:1–17.
[18] Caiazzo F, Caggiano A. Laser direct metal deposition of 2024 Al alloy: trace geometry prediction via machine learning. Materials 2018;11(3):444.
[19] Jeon I, Yang L, Ryu K, Sohn H. Online melt pool depth estimation during directed energy deposition using coaxial infrared camera, laser line scanner, and artificial neural network. Addit Manuf 2021;47:102295.
[20] Qi X, Chen G, Li Y, Cheng X, Li C. Applying neural-network-based machine learning to additive manufacturing: current applications, challenges, and future perspectives. Engineering 2019;5(4):721–9.
[21] Sing SL, Kuo CN, Shih CT, Ho CC, Chua CK. Perspectives of using machine learning in laser powder bed fusion for metal additive manufacturing. Virtual Phys Prototyp 2021;16(3):372–86.
[22] Tian C, Li T, Bustillos J, Bhattacharya S, Turnham T, Yeo J, et al. Data-driven approaches toward smarter additive manufacturing. Adv Intell Syst 2021;3(12):2100014.
[23] Meng L, McWilliams B, Jarosinski W, Park HY, Jung YG, Lee J, et al. Machine learning in additive manufacturing: a review. JOM 2020;72(6):2363–77.
[24] Gan Z, Li H, Wolff SJ, Bennett JL, Hyatt G, Wagner GJ, et al. Data-driven microstructure and microhardness design in additive manufacturing using a self-organizing map. Engineering 2019;5(4):730–5.
[25] Baturynska I, Martinsen K. Prediction of geometry deviations in additive manufactured parts: comparison of linear regression with machine learning algorithms. J Intell Manuf 2021;32:179–200.
[26] Maleki E, Bagherifard S, Guagliano M. Application of artificial intelligence to optimize the process parameters effects on tensile properties of Ti–6Al–4V fabricated by laser powder-bed fusion. Int J Mech Mater Des 2022;18:199–222.
[27] Li J, Zhou Q, Huang X, Li M, Cao L. *In situ* quality inspection with layer-wise visual images based on deep transfer learning during selective laser melting. J Intell Manuf 2023;34:853–67.
[28] Scime L, Beuth J. A multi-scale convolutional neural network for autonomous anomaly detection and classification in a laser powder bed fusion additive manufacturing process. Addit Manuf 2018;24:273–86.
[29] Caggiano A, Zhang J, Alfieri V, Caiazzo F, Gao R, Teti R. Machine learning-based image processing for on-line defect recognition in additive manufacturing. CIRP Ann 2019;68(1):451–4.
[30] Mohammadi MG, Mahmoud D, Elbestawi M. On the application of machine learning for defect detection in L-PBF additive manufacturing. Opt Laser Technol 2021;143:107338.
[31] Schmid S, Krabusch J, Schromm T, Jieqing S, Ziegelmeier S, Grosse CU, et al. A new approach for automated measuring of the melt pool geometry in laser-powder bed fusion. Prog Addit Manuf 2021;6(2):269–79.
[32] Scime L, Beuth J. Using machine learning to identify *in-situ* melt pool signatures indicative of flaw formation in a laser powder bed fusion additive manufacturing process. Addit Manuf 2019;25:151–65.
[33] Bag S, De A, DebRoy T. A genetic algorithm-assisted inverse convective heat transfer model for tailoring weld geometry. Mater Manuf Process 2009;24(3):384–97.
[34] Das D, Pratihar DK, Roy GG, Pal AR. Phenomenological model-based study on electron beam welding process, and input–output modeling using neural networks trained by back-propagation algorithm, genetic algorithms, particle swarm optimization algorithm and bat algorithm. Appl Intell 2018;48(9):2698–718.
[35] Johnson NS, Vulimiri PS, To AC, Zhang X, Brice CA, Kappes BB, et al. Invited review: machine learning for materials developments in metals additive manufacturing. Addit Manuf 2020;36:101641.
[36] Wang B, Tao F, Fang X, Liu C, Liu Y, Freiheit T. Smart manufacturing and intelligent manufacturing: a comparative review. Engineering 2021;7(6):738–57.
[37] Gunasegaram DR, Murphy AB, Barnard A, DebRoy T, Matthews MJ, Ladani L, et al. Towards developing multiscale–multiphysics models and their surrogates for digital twins of metal additive manufacturing. Addit Manuf 2021;46:102089.
[38] Wei HL, Liu FQ, Liao WH, Liu TT. Prediction of spatiotemporal variations of deposit profiles and inter-track voids during laser directed energy deposition. Addit Manuf 2020;34:101219.
[39] Liu FQ, Wei L, Shi SQ, Wei HL. On the varieties of build features during multi-layer laser directed energy deposition. Addit Manuf 2020;36:101491.
[40] Wei HL, Liu FQ, Wei L, Liu TT, Liao WH. Multiscale and multiphysics explorations of the transient deposition processes and additive characteristics during laser 3D printing. J Mater Sci Technol 2021;77:196–208.
[41] Ren K, Chew Y, Liu N, Zhang YF, Fuh JYH, Bi GJ. Integrated numerical modelling and deep learning for multi-layer cube deposition planning in laser aided additive manufacturing. Virtual Phys Prototyp 2021;16(3):318–32.
[42] Gu D, Ma C, Xia M, Dai D, Shi Q. A multiscale understanding of the thermodynamic and kinetic mechanisms of laser additive manufacturing. Engineering 2017;3(5):675–84.
[43] Du Y, Mukherjee T, DebRoy T. Physics-informed machine learning and mechanistic modeling of additive manufacturing to reduce defects. Appl Mater Today 2021;24:101123.
[44] Yang T, Liu T, Liao W, MacDonald E, Wei H, Chen X, et al. The influence of process parameters on vertical surface roughness of the AlSi10Mg parts fabricated by selective laser melting. J Mater Process Technol 2019;266:26–36.
[45] Yale K. Preparing the right data diet for training neural networks. IEEE Spectr 1997;34(3):64–6.
[46] Wang J, Li S, An Z, Jiang X, Qian W, Ji S. Batch-normalized deep neural networks for achieving fast intelligent fault diagnosis of machines. Neurocomputing 2019;329:53–65.
[47] Abadi M, Agarwal A, Barham P, Brevdo E, Chen Z, Citro C, et al. TensorFlow: large-scale machine learning on heterogeneous distributed systems. 2016. arXiv:1603.04467v2.
[48] Bircanoğlu C, Arıca N. A comparison of activation functions in artificial neural networks. In: Proceedings of the 26th Signal Processing and Communications Applications Conference (SIU); 2018 May 2–5; Izmir, Turkey. IEEE; 2018. p. 1–4.
[49] He S, Guo F, Zou Q, Ding H. MRMD2.0: a python tool for machine learning with feature ranking and reduction. Curr Bioinform 2020;15(10):1213–21.
[50] Ruder S. An overview of gradient descent optimization algorithms. 2016. arXiv:1609.04747.
[51] Wu X, Zheng W, Chen X, Zhao Y, Yu T, Mu D. Improving high-impact bug report prediction with combination of interactive machine learning and active learning. Inf Softw Technol 2021;133:106530.

[52] Klawonn M, Heim E, Hendler J. Exploiting class learnability in noisy data. Proc AAAI Conf Artif Intell 2019;33(1):4082–9.
[53] Zheng W, Liu X, Yin L. Research on image classification method based on improved multi-scale relational network. PeerJ Comput Sci 2021;7:e613.
[54] Khairallah SA, Sun T, Simonds BJ. Onset of periodic oscillations as a precursor of a transition to pore-generating turbulence in laser melting. Addit Manuf Lett 2021;1:100002.
[55] Gan Z, Kafka OL, Parab N, Zhao C, Fang L, Heinonen O, et al. Universal scaling laws of keyhole stability and porosity in 3D printing of metals. Nat Commun 2021;12:2379.
[56] Khairallah SA, Martin AA, Lee JRI, Guss G, Calta NP, Hammons JA, et al. Controlling interdependent meso-nanosecond dynamics and defect generation in metal 3D printing. Science 2020;368(6491):660–5.
[57] Matthews MJ, Guss G, Khairallah SA, Rubenchik AM, Depond PJ, King WE. Denudation of metal powder layers in laser powder bed fusion processes. Acta Mater 2016;114:33–42.
[58] Lee S, Peng J, Shin D, Choi YS. Data analytics approach for melt-pool geometries in metal additive manufacturing. Sci Technol Adv Mater 2019;20(1):972–8.
[59] Mukherjee T, Debroy T. A digital twin for rapid qualification of 3D printed metallic components. Appl Mater Today 2019;14:59–65.
[60] Knapp GL, Mukherjee T, Zuback JS, Wei HL, Palmer TA, De A, et al. Building blocks for a digital twin of additive manufacturing. Acta Mater 2017;135:390–9.
[61] Tao F, Qi Q, Wang L, Nee AYC. Digital twins and cyber–physical systems toward smart manufacturing and Industry 4.0: correlation and comparison. Engineering 2019;5(4):653–61.